University of Crete
Department of Materials Science
and Technology

First-principle simulations for transition-metal dichalcogenide alloys

Author:
Michael Minotakis

Thesis Committee:
Ioannis N. Remediakis
(supervisor)
Georgios Kopidakis
George Kioseoglou

-

March 20, 2019

Contents

List of Figures

Abstract

During the last decade, researchers have focused on two-dimensional layers of Transition Metal Dichalcogenides, MX_2 where M is group IV transition metal and X is a chalcogen (S, Se, Te). Recently, it has been established that all materials in this family are semiconductors with metallic edges.

An open question is how to modify these materials so that their properties, such as their band gap satisfy the corresponding applications. The main methods that have been employed to this end are nanostructuring, strain and alloying.

In this thesis, we study alloying in 2D and 1D nanostructures. We developed a method that produces not only reliable results but also is very computationally efficient. Our methodology is based on Density Functional Theory for the electronic structure and the Virtual Crystal Approximation for creating model alloys. We studied how the electronic properties and structural parameters of the 2D materials depend on the concentration of the alloying material. We have confirmed our results through test calculations with more accurate models.

We employ this method to simulate the effect of alloying on the properties of nanoribbons and study how the metallic states depend on the composition of the nanoribbon. Also, we find significant Fermi level pinning of the metallic edge compared to the interior. Furthermore, we studied how the edge energy changes with composition. Last but not least, we compared the properties of segregated versus random alloys.

1 Introduction

In this thesis, we performed Density Functional Theory [1] calculations for two dimensional transition metal dichalcogenide alloys [2] and nanoribbons. Two dimensional materials [3] are an expanding area of research for the materials science since the discovery of graphene. In this thesis we focus on the study of transition metal dichalcogenides (TMD) [4] [5]. In this thesis, we focus on two dimensional alloys and nanoribbons of these alloys, and use virtual crystal approximation to simulate their properties.

1.1 Computational Science

The study of a physics problem often requires the solution of difficult equations, which are frequently non-solvable via analytical methods (for example, in this study we need to solve the Schrödinger equation). In order to solve such types of problems, except of making reasonable approximations (for example Born- Oppenheimer approximation), we make use of numerical methods such as the Monte Carlo integration, Simplex algorithm method and many others. Computational Science therefore is the science that uses numerical analysis in order to solve a problem for which a quantitative theory already exists.

In recent years, because of the rapid evolution of computers, computational science has experienced great progress. Additionally, the advantages of computational science are many. First of all, researchers can arrive at conclusions through the use of computers, saving considerable amount of time and resources. Furthermore, we can study many problems through simulations which cannot be studied experimentally, due to extreme conditions such as high temperature, pressure, lack of technology etc. Computational science is widely used in physics, biology, materials science and other topics.

1.2 Two-dimensional Materials

Two-dimensional materials, often referred to as "Single-Layer materials", are crystalline materials consisting of a single layer of atoms. The most famous of these materials is graphene [3] which is a single layer of graphite in which the carbon atoms form a hexagonal lattice. Since the isolation of graphene in 2004, a large amount of research has been directed in the study of these materials [2, 6], and in 2010 the Nobel Prize was awarded to the researchers that pioneered its research, Andre Geim and Konstantin Novoselov. Additionally, these materials have a wide range of applications such as photovoltaics, photo detectors and sensors, just to name a few.

1.2.1 Introduction to TMDs

Transition-metal-dichalcogenide monolayers are atomically thin semiconductors of the general type MX_2 where M is the *Transition Metal* atom such as Molybdenum (Mo) and Tungsten (W) and X is the *Chalcogen* atom such as Sulphur (S) , Selenium (Se) and Tellurium (Te). This structure is made by a layer of transition metal which is among two layers of chalcogen as we can see in the Fig. 1 . Transition metal dichalcogenide bulk crystals (3-D) are formed of monolayers bound to each other by Van Der Waals interactions, as shown in Fig. 1.

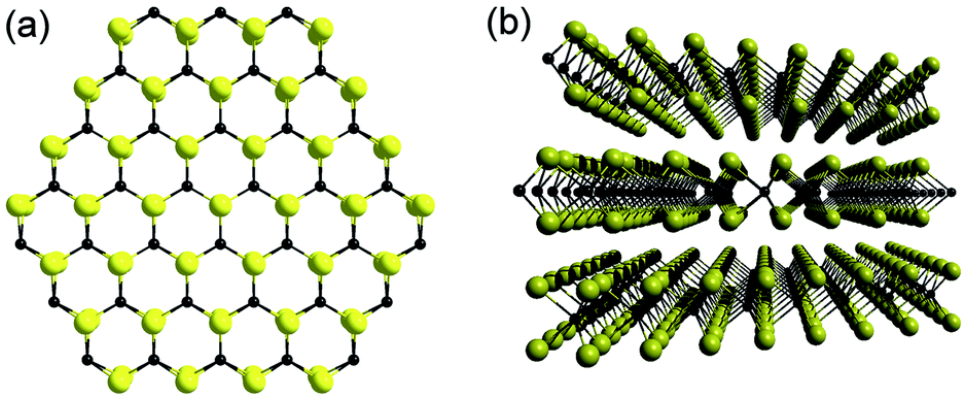

Figure 1: (a) Top view of honeycomb lattice. (b) Side view of MX_2 monolayers. Black balls are the Transition Metal atoms and the yellow are the Chalcogen atoms (images taken from [7])

Depending on the transition metal atom, interatomic distances in the MX_2 layer may vary. In general terms, the distances increase when the transition metal atom is heavier. Also, distances increase as we introduce heavier chalcogens in the lattice. The smallest distances therefore are observed in MoS_2 and the largest is the WTe_2.

Transition metal dichalcogenides are known for their significant optoelectronic properties [6]. Monolayers have a direct gap and can be used in electronics as transistors and in optics as emitters and detectors [8]. Also, TMD monolayer crystal structures have no inversion center, which allows to access a new degree of freedom of charge carriers. Also, the mechanical properties that TMD monolayer structures have are quite notable. A monolayer of MoS_2 can be strained up to 25% and the band gap is a function of the applied strain [9]. TMDs are materials that are used in catalysis, as we knew already from mid $90's$ [10] and are great lubricants, as we know from early $70's$ [11].

1.3 Transition Metal Dichalcogenide Alloys

After the vast expansion of the 2D materials as an area of research of materials science, many researchers have focused on tuning their electronic properties and especially the band gap. Alloying or doping is the obvious way to tune the electronic structure. One of the first works [2] in 2012 used ab initio simulations for transition-metal-dichalcogenide alloys and reported the tuneable band gap as a function of concentration. The main result of this work is shown in Fig. 2. The band gap of these materials changes non-linearly with doping.

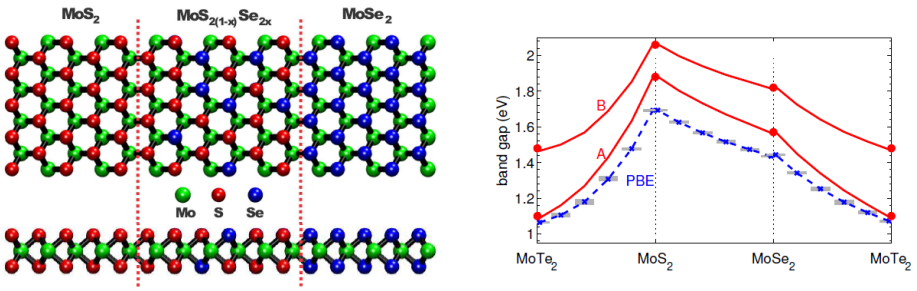

Figure 2: Atomic structure (left) and band gap (right) of MoX_2 alloy as a function of the concentration. Dashed lines are calculation band gaps and the two solid lines correspond to the experimentally resolved A and B optical transitions. Fig. 2 from [2]

A combined experimental and theoretical work was published on 2014 about the alloy $MoS_{2x}Se_{2(1-x)}$. The alloy was grown via chemical vapor deposition. Triangular nanosheets were formed. By means of photoluminescense, spectroscopy and DFT calculation, the researchers found an almost linear dependence of band gap on the amount of S in the alloy, as shown in Fig. 3 [12]:

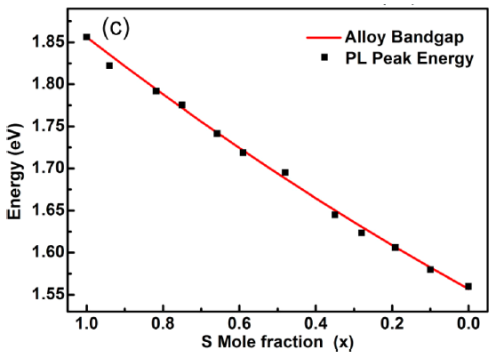

Figure 3: Band gap of $MoS_2Se_{2(1-x)}$ alloys as a function of the composition,x, for the MoX_2 nanosheets. Adapted from [12]

In 2017, Susarla et al. reported the making of the quaternary alloy $Mo_xW_{1-x}S_{2x}Se_{2(1-x)}$ via chemical vapor deposition method and studied the band gap as a function of the composition. The main finding of this research is the high tunability of the band gap for these materials. The alloy was studied both theoretically and experimentally. In Fig. 4, we see the band gap of these quaternary alloys as a function of the composition and the band structure of $Mo_{0.50}W_{0.50}S_2$ [13].

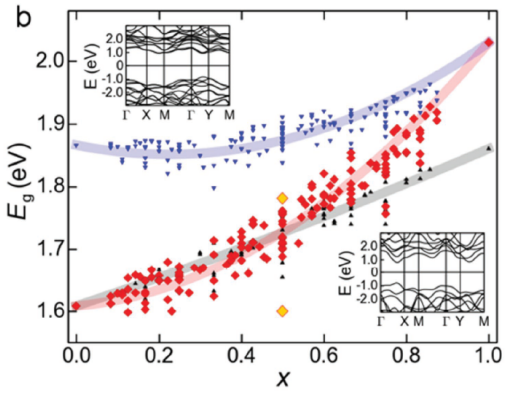

Figure 4: Band gaps of the quaternary alloy $Mo_xW_{1-x}S_{2x}Se_{2(1-x)}$ (red diamonds), binary $W_xMo_{1-x}S_2$ and $MoS_{2x}Se_{2(1-x)}$ alloys are shown by small blue downward and black upward triangles, respectively. Also, band structure of alloys $Mo_{0.50}W_{0.50}S_2$ with the largest and smallest bandgaps are shown on top left and bottom right. Adapted from [13].

All calculations discussed in the previous paragraphs have used the supercell method to calculate the band gap. This is a computational expensive method that uses large supercells with many atoms and many different structures. For example, in [13], 152 different structures were used for the quaternary alloy. Also, a detailed study of the characteristics of the structure as a function of the concentration is missing as this is very difficult task for supercell structures.

Here, we use a method (VCA) that it is very quick and also not computationally expensive, because it is applied to the smallest possible supercell of three atoms. In the first part of the thesis, we exploit the validity of the method in comparison to the more accurate methods. We identify the systems where this method can be a fast tool that we can use in order to produce reliable data.

Having established the validity of the methods, we then apply it to nanostructures. To study nanoribbon alloys, one would need supercells containing of the order of 1000 atoms, which are impossible to study with DFT. In chapter 5, we demonstrate the study of nanoribbon alloys with VCA using supercells that contain few tens of atoms.

1.4 TMD Nanoribbons

TMD nanoribbons are 1D structures that show very interesting electronic properties. The most widely studied are zig-zag edge nanoribbons of MoS_2, with two S adatoms on the Mo edge [14]. These nanoribbons exhibit metallic character on their edges [15]. They consist of a semiconducting bulk that has metallic character in the edges. The density of states graph (DOS) that verifies this is shown in Fig. 4. The Fermi level is found to be lower than that of the 2D material.

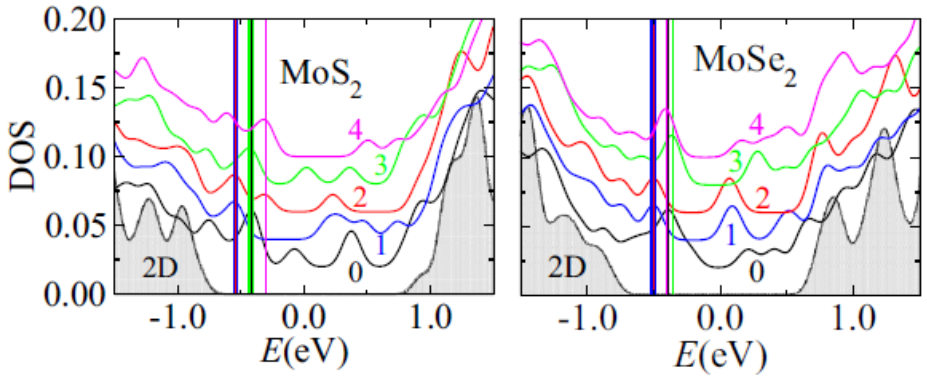

Figure 5: Density of states graph for the MoS_2 and $MoSe_2$ nanoribbon with N adatoms (N shown above each curve). The vertical lines denote position of the Fermi energy. The shaded part is the DOS graph of the corresponding 2D material. Adapted from Ref. [14].

In this thesis, we employ virtual crystal approximation in order to simulate the alloying on these nanoribbons and study how these states change with the composition. Also,we study this metallic character as we change the composition of the materials, and find the Fermi level pinning of the nanoribbons.

2 Electronic structure calculations

In this section, we give a brief introduction of the basic theory of the many-electron problem, the *Density Functional Theory* [1] and the *Hartree -Fock Method* [16]. Both theories are simplifications of the full problem of many electrons moving in a potential field.

2.1 The Born- Oppenheimer approximation and single-electron equations

Every quantum mechanical phenomenon is described by the Schrödinger equation.

$$\hat{H}\Psi = E\Psi \tag{1}$$

Where:
$\hat{H}$ is the *Hamiltonian Operator* (described in Eg.(2)).
Ψ is the *Wavefunction*.

For a system of N electrons and K nuclei with charges Z_n the Hamiltonian Operator is :

$$\begin{aligned}\hat{H}_{tot} = &\sum_{i=1}^{N} \frac{\hat{p_i}^2}{2m} + \sum_{n=1}^{K} \frac{\hat{P_n}^2}{2M_n} + \frac{1}{8\pi\varepsilon_0} \sum_{i,j=1;i\neq j} \frac{e^2}{\left|\vec{r_i} - \vec{r_j}\right|} \\ &- \frac{1}{4\pi\varepsilon_0} \sum_{n=1}^{K}\sum_{i=1}^{N} \frac{Z_n e^2}{\left|\vec{r_i} - \vec{R_n}\right|} + \frac{1}{8\pi\varepsilon_0} \sum_{n,n'=1;n\neq n'}^{K} \frac{Z_n Z_{n'} e^2}{\left|\vec{R_n} - \vec{R_{n'}}\right|}\end{aligned} \tag{2}$$

in which the i index refers to the electrons and the n to the nuclei, m is the mass of electrons and M_n is the mass of different nuclei. In order to solve this equation we must make some approximations. The first one is called *Born-Oppenheimer approximation [16]* which assumes that electrons move under constant nuclei positions. This assumption is made because the nucleus is much heavier than the electron so nuclei move more slowly than electrons. The Born Oppenheimer Hamiltonian is :

$$\mathcal{H} = \sum_{i=1}^{N} \frac{\hat{p_i}^2}{2m} + \frac{1}{8\pi\varepsilon_0} \sum_{i,j=1;i\neq j} \frac{e^2}{\left|\vec{r_i} - \vec{r_j}\right|} - \frac{1}{4\pi\varepsilon_0} \sum_{n=1}^{K}\sum_{i=1}^{N} \frac{Z_n e^2}{\left|\vec{r_i} - \vec{R_n}\right|} \tag{3}$$

Although the Born-Oppenheimer approximation offers a great simplification, the Hamiltonian is still unsolvable due to the correlation between electron positions in the second term of Eq. (2).

It is desirable to reduce the degrees of freedom and approximate H with a sum of one electron Hamiltonians which is a solvable problem . If this was possible, the resulting *independent-particle (IP)* Hamiltonian has the form:

$$\mathcal{H} = \sum_{i=1}^{N} H(\vec{p_i}, \vec{r_i}) \tag{4}$$

Even then, the form of this Hamiltonian can be quite complicated because the potential depends of the wave function ψ on which the Hamiltonian is acting.

An approximation of the many electron problem is the Hartree-Fock Method [16]. This method is a variational method in which the electron wave functions of the system have the form of an antisymmetrised product of one electron wave functions (it is antisymetrical due to the fermion character of the electron). So the restrictions lead to an effective Schrödinger equation for the individual one electron wave functions. The solution is found iteratively in a self-consistent procedure.

The vast majority of electronic structure calculations is performed today using Density Functional Theory (DFT). This method is described in detail in the next section.

2.1.1 Density Functional Theory

Density Functional Theory results from the work of Hohenberg, Kohn and Sham [17] [18]. Nowadays, most structure calculations for solids and nanostructures are based on Density Functional Theory. In DFT, the electonic orbitals are solutions to a Schrödinger equation where the potential energy depends on the electron density.

The fundamental theorem of density functional theory is that all properties of a system of many interacting particles are functionals of the ground state electron density, $n(\vec{r})$. Therefore the density contains information of the many body wave functions for the ground state and all excited states. Moreover, the system can be described by a single particle hamiltonian in (3):

$$H = \hat{T}_e + \hat{V}_{n-e} + \hat{V}_{e-e} + \hat{V}_{xc} \tag{5}$$

Where:
$\hat{T}_e$: is the operator for the *Kinetic energy of electron.*
$\hat{V}_{n-e}$: is the operator for the *Potential energy* through the Coulomb interactions of the nucleus and electron.
$\hat{V}_{e-e}$: is the operator for the *Potential energy* through Coulomb interaction of the electrons.
$\hat{V}_{xc}$: is the Exchange Correlation Potential energy Operator that exists only in the single particle Hamiltonian.

The fourth term of the Hamiltonian, the *Exchange Correlation Potential* contains together the many body effects. This term corrects of the electron self-interaction which leads to the overestimated electron-electron interaction. Also, it contains the Pauli exclusion principle (exchange) and the corellation between the electron positions. We cannot have simple accurate expressions. For example two common approximations are local density approximation (LDA) and the generalized gradient approximation (GGA).

The electron density is the key function in DFT, as the V_{e-e} and V_{xc} potentials are functionals of the density. It satisfies the relationship.

$$N = \int n(\vec{r})\, d^3r, \tag{6}$$

and it must be self consistent with the single electron wave functions that are eigenfunctions of the hamiltonian of Eq. (5):

$$n(\vec{r}) = \sum_{i=1}^{N} \left|\Psi_i(\vec{r})\right|^2 \tag{7}$$

The Ψ_i satisfy a generalized Schrödinger equation that is called the Kohn-Sham equation:

$$\left[-\frac{\hbar^2}{2m_e}\sum_i \nabla_i^2 + V_{n-e} + \frac{e^2}{4\pi\varepsilon_0}\int d^3r' n(\vec{r'})\frac{1}{\left|\vec{r}-\vec{r'}\right|} + V_{xc}(\vec{r})\right]\Psi_i(\vec{r}) = E_i\Psi_i(\vec{r}) \tag{8}$$

Many functionals have been developed for the exchange correlation potential, such as the GGA (generalized gradient approximation), LDA (local density approximation) and more. For the purpose of this study we will use the GGA functional and specifically the Perdew-Burke-Ernzenhof functional.

Local Density Approximation LDA is an approximation for the exchange correlation energy functional that assumes that the X-C energy at each point of space equals to the X-C energy of a homogeneous system, $\varepsilon_{xc}^{hom}(n)$, of density n. The equation that defines this approximation is:

$$E_{xc}^{LDA}[n] = \int n(\vec{r})\varepsilon_{xc}^{gas}(n(\vec{r}))d^3r \tag{9}$$

$\varepsilon_{xc}^{gas}(n)$: is the exchange correlation energy per particle of an homogeneous electron gas with density of n.

Generalized Gradient Approximation

In this approximation we make the hypothesis that the exchange-correlation potential energy is a function of the electron density and the gradient of it, as shown in the next equation:

$$E_{xc}^{GGA}[n] = \int n(\vec{r})\varepsilon_{xc}^{GGA}(n, \nabla n)d^3r \tag{10}$$

Generalized gradient approximation calculates the exchange correlation energy taking into account both electron-density and the gradient of electron density so we have better results. This method provides more accurate results than LDA while being about two times slower in realistic simulations.

Perdew-Burke-Ernzenhof GGA PBE [19] is a numerical approach to the general gradient approximation in which the exhange correlation energy is in the form:

$$E_{xc}^{GGA}[n] = \int n(\vec{r})\varepsilon_{x}^{unif}(n)F_{xc}(r_s, s)d^3r \tag{11}$$

where:
r_s is the Seitz radius ($n^{-1} = \frac{3}{4}\pi r_s^3$).
$s = \frac{\nabla n}{2k_F n}$ is a dimensionless density gradient where $k_F = (3\pi^2 n)^{1/3}$.
$F_{xc}(r_s, s)$ is the enchancement factor.

2.1.2 Pseudopotentials

The general idea of the pseudopotential term is the replacement of the strong Coulomb potential of the nucleus and the effects of the tightly bound core electrons by an effective ionic potential acting on the valence electrons. Pseudopotentials are not unique, and there is some freedom to choose whatever is suitable for each calculation. The most popular choices are *ab initio norm-conserving* and *ultrasoft* pseudopotentials. The main goal for the ultrasoft pseudopotential is to create pseudofunctions that are as smooth as possible, yet are accurate. On the other hand, *Norm-Conserving* pseudopotentials focus more on accuracy, but at some sacrifice of smoothness. The fundamental constraint of these pseudopotentials is that all-electron and pseudo wavefunctions are identical outtside the cut off radius. Pseudopotentials are the basis for much of the current research and development of new methods in electronic structure. An example of the use of pseudopotential is shown in Fig. 6.

Pseudopotential is an operator, not just a potential energy function. It is defined as

$$V_{PP} = V_{PS}(\vec{r}) + \sum_{i}^{core} (\epsilon - \epsilon_i) \left|i\right\rangle \left\langle i\right| \tag{12}$$

where $|i\rangle$ is the all-electron core states with $\psi^{AE}(r) = \langle r|i\rangle$. Therefore the pseudopotentia operator depends on the energy of the state that it acts on. Usually, $|i\rangle$ are expanded into the solutions of the Schrödinger equation for the spherical well, which are $J_l(kr)Y_{lm}(\theta, \phi)$ where J_l is spherical Bessel function and Y_{lm} spherical harmonic.

Norm-Conserving Pseudopotentials Pseudopotentials that are generated by calculations on atoms and not by fit in experimental data are called ab-initio. The norm conservation [20] that proposed by Hamann, Schlüter and Chang in 1979 is essential to make this type of pseudopotentials more accurate and transferable. This type of pseudopotentials are constructed to enforce one condition.

Inside the cut-off radius the norm of each pseudo wavefunction should be identical to all-electron wavefunction.

Ultrasoft Pseudopotentials In order to do so, *Ultrasoft Pseudopotential* method employs a transformation that re-expresses the problem in terms of a smooth function and an auxiliary function around each ion core that represent the rapidly varying part of the density. In a calculation that uses an *ultrasoft pseudopotential*, the solutions for the smooth functions are orthonormalized according to:

$$\langle \widetilde{\psi}_i | \widehat{S} | \widetilde{\psi}_{i'} \rangle = \delta_{i'i} \tag{13}$$

where $\hat{S}$ is the overlap operator. Also, each smooth pseudofunction $\widetilde{\psi}_s$ can be formed independently, with only the constraint of matching the value of the functions $\widetilde{\psi}_s(R_c) = \psi^{AE}(r_{cut})$ at the radius r_{cut}.In this study we used **GBRV**(**G**arrity, **B**ennett, **R**abe, **V**anderbilt) ultrasoft pseudopotentials. [21] [22]

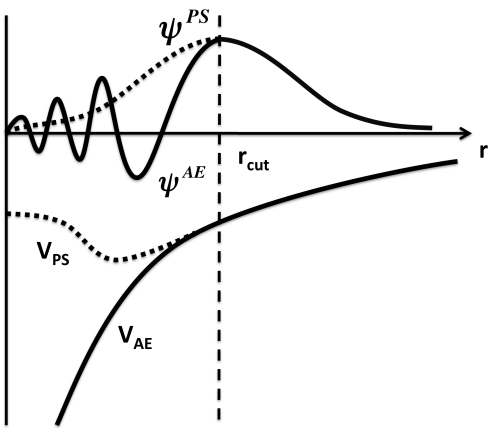

Figure 6: All electron potential (V_{AE}) and wave function, also we can see the pseudopotential (V_{PS}) and the pseudo wave function $\psi(s)$.Note that the pseudo wave function and the wave function are the same after a core radius. (images taken from [23])

2.2 Computational Parameters

2.2.1 Bloch's Theorem and Plane Wave Basis Sets (Plane wave Cut off)

When handling the problem of the infinite number of interacting electrons moving in the static field of an infinite number of ions, we have two difficulties to overcome : the first one is that a wave function has to be calculated for each of the infinite number of electrons which will extend over the entire space of the solid, the second one is that the basis set in which the wave function will be expressed should be infinite.

The ions in a perfect crystal are arranged in a regular periodic way. Therefore, the external potential felt by the electrons will also be periodic, the period is the same as the length of the unit cell (L). So the external potential on an electron at position r can be expressed as $V(r) = V(r + L)$, which is the condition for the use of Bloch's theorem [24]. With the use of this theorem it is possible to express the wave functions of the infinite crystal in terms of wave function at reciprocal space vectors of a *Bravais Lattice*.

Bloch's theorem uses the periodicity of a crystal to reduce the infinite number of electron wave functions to be calculated, on simply the number of electrons in the unit cell of the crystal. The wave function is written as the product of a cell periodic part and a wavelike part.

$$\Psi_i(\vec{r}) = e^{i\vec{k}\vec{r}} f_i(\vec{r}) \tag{14}$$

in which the $f_i(\vec{r})$ is a periodic function with the periodicity of the unit cell. The Fourier series fo $f_i(\vec{r})$ is

$$f_i(\vec{r}) = \sum_G c_{i,G} e^{i\vec{G}\vec{r}}, \tag{15}$$

where $\vec{G}$ are the reciprocal lattice vectors; for one dimensional lattice they are $G = \frac{2\pi m}{L}$. Therefore, each electronic wavefunction is written as a sum of plane waves:

$$\Psi_i(\vec{r}) = \sum_G c_{i,k+G} e^{i(\vec{k}+\vec{G})\vec{r}} \tag{16}$$

The electronic wavefunction at each k-point is now expressed in terms of a discrete plane wave basis set. In principle, this Fourier series is infinite, but the terms become smaller for large values of $\left|\vec{G}\right|$. We can assign to each plane wave a kinetic energy $\frac{\bar{h}^2(|\vec{k}+\vec{G}|)^2}{2m}$. The plane waves with a smaller kinetic energy typically have a more important role than those with a very high kinetic energy. Defining a *plane wave energy cut off* (E_c) reduces the basis set to a finite size. In Eq. 16 we only use terms for which

$$\frac{\hbar^2\left|\vec{k}+\vec{G}\right|^2}{2m} \leq E_c \tag{17}$$

2.2.2 Number of points in Brillouin Zone (k-points)

Using Bloch's theorem we can write the electron wave function as a product of a plane wave and a periodic function (equation (14)). So, one of the parameters that play a major role in this study is the number of k-points [24]. All physical properties in the system are periodic functions of the eigenstates of the $\vec{k}$ vector. We only need to consider $\vec{k}$ vectors inside the primitive unit cell of the reciprocal lattice of the system, which is called Brillouin Zone. For example, in one dimension, we just have to take the k-points that are in the range between $\frac{-\pi}{a} \leq k \leq \frac{\pi}{a}$ where a is the lattice constant. In Fig. 7 we see the graphical representation of characteristic k-points for the first Brillouin Zone for some common Bravais Lattices:

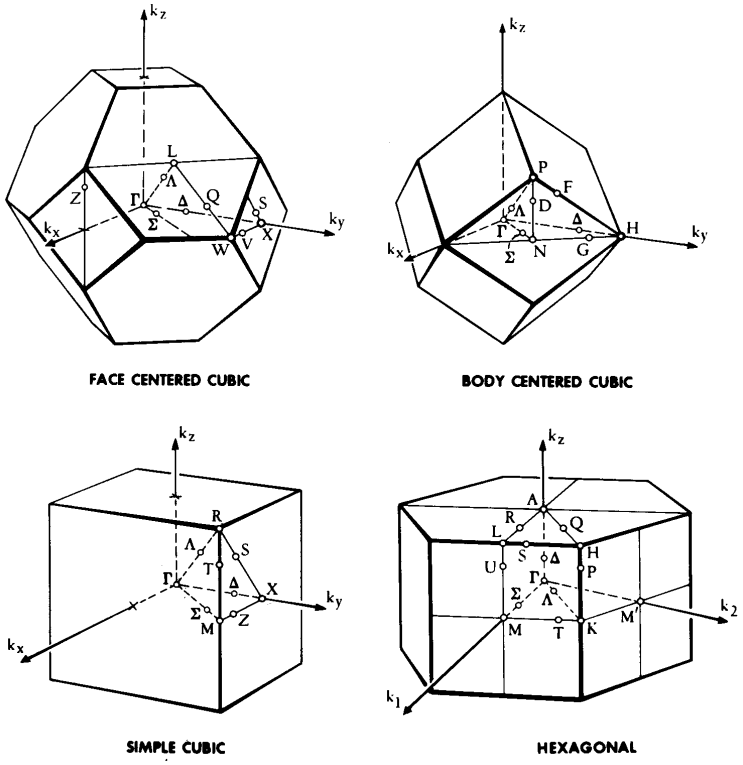

Figure 7: First Brillouin zone for some common Bravais Lattices : fcc,bcc,sc,hcp. Images taken from [24]

The Brillouin zone is sampled by a set of so-called special k-points that form a grid in the reciprocal space. For example a $4 \times 4 \times 2$ grid corresponds

to 32 special k-points. In practice, a smaller set of k-points is used because the symmetry of the crystal is taken into account. For example, in a cubic crystal, the k-points (k,0,0), (0,k,0), (0,0,k) correspond to wavefunction with the same energy.

2.3 Virtual Crystal Approximation

The direct approach to simulate the properties of an alloy is the use of the supercell method. In the supercell alloy method, one creates a simulation cell with many atoms (between 10 and 100), and substitutes a number of them with the alloying element. For each composition, a large number (between 3 and 10) of supercells is created to account for different configurations of the atoms; for example, two atoms of the alloying element might be neighbours or second neighbours or at a larger distance. In this method, one builds a supercell of the compounds and then performs statistical analysis of the data due to the many different configurations. This method, as it can be easily understood, costs a lot on computational resources. Also, these methods generally require the use of very large supercells, just to simulate a small area of the material.

Therefore, it is very desirable to find a simpler and computationally less expensive method to simulate alloys. One such method implies the use of virtual crystals [25], in which we have the same periodicity as the primitive crystal but we change the atoms with virtual atoms which interpolate between the parent atoms. This method, called Virtual Crystal Approximation (VCA), was developed in 1991 to simulate Si_xGe_{1-x} alloys with DFT [26]. The so called "virtual atoms" are not a simple average of the constituting elements: Obviously, a $50\% - 50\%$ alloy of Si (Z=14) and Ge (Z=32) is not equivalent tobulk Cr (Z=24, the average of 14 and 32). The virtual $Si_{0.5}Ge_{0.5}$ atom is an atom with four valence electrons and sp^3 orbitals, such as Si and Ge, where the energies of these electrons are the average of the coresponding energies of valence electrons in Si and in Ge.

Apart from the obvious advantages, one disadvantage is that this method is not as accurate as the supercell method. However, researchers have stated that this method is in good agreement with other much more complicated methods in several prototypical systems such as Si_xGe_{1-x} [27]. VCA is mostly efficient for atoms of the same column of the periodic table that have same number of valence electrons.

In order to simulate an alloy of the chemical formula $A_{1-x}B_x$, the virtual potential is made by averaging the potentials of the parent compounds.

$$V_{VCA} = (1 - x)V_A + xV_B \tag{18}$$

In practice, the previous summation is usually done in Fourier space by averaging the corresponding potentials ($V_A(\boldsymbol{G})$ and $V_B(\boldsymbol{G})$).

2.4 BFGS method

In this thesis, all properties that we are going to examine will be calculated in the ground state, which is the configuration with the lowest total energy. In order to obtain the ground state we need to relax the whole structure. For this work, we are going to use variable cell relaxation and atom relaxation. The heart of this processes is located in the BFGS algorithm of Broyden–Fletcher–Goldfarb–Shanno algorithm [28].

This algorithm is an iterative method to solve unstrained nonlinear optimization problems. This method belongs to the quasi-Newton methods family. It is a hill climbing optimization technique which seeks for a stationary point of a function. For this type of problem, a necessary condition for optimality is that the gradient should be zero. Quasi - Newton methods are generalizations of the secant method to find the root of the first derivative for multidimensional problems.

Suppose we need to find minimum of a function $f(x)$, where $x = (x_1, x_2, x_3, ...)$. The method starts with an initial guess (x_0) and an Hessian matrix B_0. Hessian matrix is defined as $B_{ij} = \frac{\partial^2 f}{\partial x_i \partial x_j}$. The steps that follow are repeated until we find a convergence to the solution x_k :

1. Find the direction p_k by solving the equation $B_k p_k = -\nabla f(x_k)$.
2. Perform line search to find a good step a_k in the direction that we found from above, i.e. find minimum value of one-variable function $f(a) = f(x_k + \alpha p_k)$.
3. Then set $s_k = a_k p_k$ and update to the $x_{k+1} = x_k + s_k$.
4. Find the difference between the gradients of the values between the first and the last value of the function, $y_k = \nabla f(k+1) - \nabla f(x_k)$
5. Change to a new Hessian matrix with the following equation:

$$B_{k+1} = B_k + \frac{y_k y_k^T}{y_k^T s_k} - \frac{B_k s_k s^T B_k}{s^T B_k s_k} \tag{19}$$

6. Go back to step 1 unless $B_{k+1} \approx B_k$

Having stated the fundamentals of this method we are going to use it in for relaxation calculations and also for variable cell relaxation calculations in order to find the structure of minimum energy for our calculations.

3 Convergence Calculations and Preparatory simulations

3.1 Convergence Calculations

In this section we are going to investigate the parameters for which our calculations are converged. The convergence criterion is that the total energy does not change before the second decimal. The parameters that we are going to investigate are the number of k-points and the plane-wave cut off. We used the unit cell of three atoms that generates the 2D surface for MoS_2 (Fig. 8). All parameters that we are going to discuss are calculated using the Quantum Espresso Software and the GBRV ultrasoft pseudopotentials [22]. We took into account the suggestions of the SSSP efficiency graphs [29].

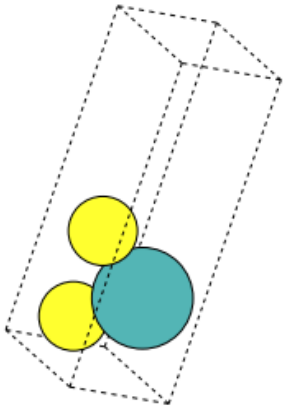

Figure 8: Unit cell of MoS_2 that generates the 2D surface. Mo in blue and S in yellow.

3.1.1 Plane-Wave Cut-off Convergence Calculations

We started from a fixed geometry of MoS_2, found in previous studies of our research group, where the distance between trantision metals is $d_{M-M} = 3.183$ Å and the distance between the chalcogens is $d_{S-S} = 3.125$ Å. Keeping everything else fixed, we modify the plane-wave cut-off (see section 2) and record the total energy of the system. The results are presented in Table 1 and in Fig. 9.

Table 1: Total energy as a function of the plane wave cut off for the MoS_2 .

Planewave cut off (eV)	**Energy(Ryd)**
300	-192.95
320	-193.02
340	-193.04
360	-193.05
380	-193.06
400	-193.07
420	-193.07
440	-193.07
460	-193.07
480	-193.07
500	-193.07
520	-193.07
540	-193.07
560	-193.07

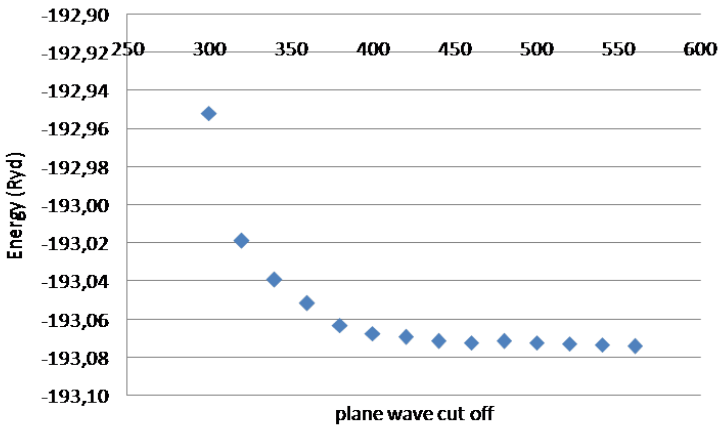

Figure 9: Total energy of MoS_2 unit cell as a function of plane wave cut off.

We clearly see that the energy converges for values above 500 eV . The Standard Solid State Pseudopotentials (SSSP) [29] efficiency graph implies a cut off of over 700 eV or 51.44 Ryd in order to have the best accuracy for our calculations, we used 725 eV or 53.074 Ry in order to be sure for our calculations accuracy not only for the total energy but also for the band gap. The next step is to calculate the number of k-points for which the energy converges.

3.1.2 K-points Mesh Calculations

In this subsection we are going to calculate the k-point mesh (see section 2) that we are going to use in the next calculations. We used the previous structure (MoS_2 with a unit cell of 3 atoms) with the plane wave cut off that we calculated previously and the GBRV ultrasoft pseudopotentials. We changed the k-points mesh until convergence fo the energy. The results are presented in Table 2 and Fig.10.

Table 2: Total energy of MoS_2 unit cell as a function of the number of k-points.

k-points	**Energy(Ryd)**
(1,1,1)	-193.07
(2,2,1)	-193.53
(3,3,1)	-193.59
(4,4,1)	-193.59
(5,5,1)	-193.59
(6,6,1)	-193.59
(7,7,1)	-193.59
(8,8,1)	-193.59
(9,9,1)	-193.59
(10,10,1)	-193.59

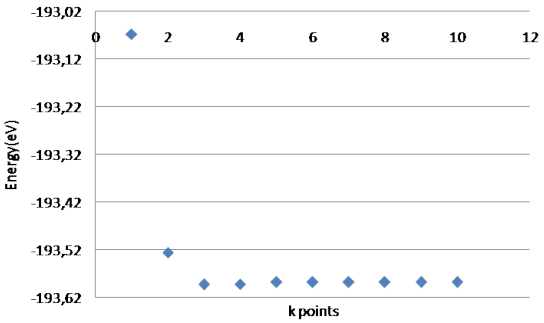

Figure 10: Total energy of MoS_2 unit cell as a function of the number of k-points.

We clearly see that the energy converges after the $(3, 3, 1)$ k-point. The band gap is more sensitive to the change of the k-point mesh [30]. To check that we performed calculations for the band gap for the alloy of $W_xMo_{1-x}S_2$ as a function of k-points. The results are shown in Fig. 11.

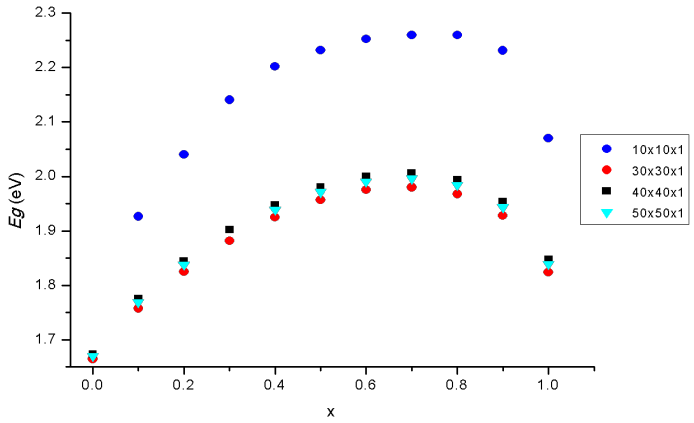

Figure 11: Band gap calculations for the alloy of $W_xMo_{1-x}S_2$ for a range of k-points values.

We clearly see now that the band gap converges for a much denser mesh of k-points of around $(30, 30, 1)$. We decided to use a mesh of $(40, 40, 1)$ for our calculations.

Having defined the basic parameters for our calculations, we test different echange and correlation functionals (see section 2.1.1) to choose which one is suitable for our calculations. Main criteria were the time of calculation and the accuracy of the outcome. We used PBE exchange correlation functional with or without Spin - Orbit Coupling; we also used LDA exchange correlation functional (PZ) we calculate the band gap for the same alloy as before. Results are shown in Fig. 12. In all cases, the lattice parameters of each material were found after full structural relaxation of the structure. To demonstrate the effect of relaxation on the band gap, we included results where the atomic positions were kept fixed.

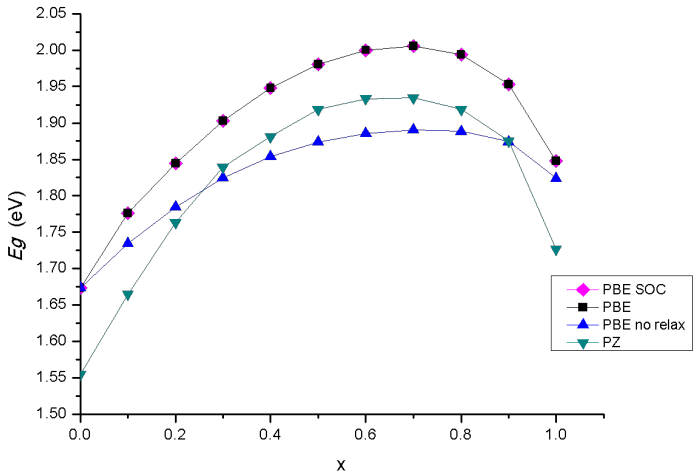

Figure 12: Band gap calculations for the alloy of $W_x Mo_{1-x} S_2$ for different methods.

We decided to use the PBE method without spin-orbit coupling, because this method was a lot faster than the others and gave us practically same band gap as the most accurate methods. While spin-orbit coupling is important for the optical properties of these materials, it does not contribute to their structural and chemical properties which is the main topic of this study. As the aim of this thesis is to study trends of parameters for nanostructures, we focus more on the reduction of the calculation time in order to make as many as possible calculations.

3.2 Tests for Virtual atoms

We have already seen the fundamentals of the virtual crystal approximation method in section 2. We now want to test the accuracy of this method for the total energy of an isolated atom. In order to study this, we calculated the energy coefficients for the parent atoms to compare it with these of the virtual atoms. We expect that the virtual atoms should have the average chemical behaviour of the parent atoms [25].

We calculated contributions to the total energy for the isolated parent atoms (Mo, W, S, Se). and for isolated virtual atoms (W_xMo_{1-x}, S_xSe_{1-x}). For each virtual atom, we compare it with the interpolated energy coefficient of the parent atom.

The definitions of the various terms in the total energy are presented briefly below. The reader is refered to specialized books such as [31] for more details. In DFT, the total energy of the system is

$$E = E_{OEC} + E_{Hartree} + E_{XC} + E_{Ewald} \tag{20}$$

where

$$E_{OEC} = \sum_{k=1}^{N} \epsilon_k \tag{21}$$

is the sum of eigenvalues of the Kohn-Sham equation (see section 2.1.1), and

$$E_{XC} = \int n(\vec{r})(\epsilon_{xc}(\vec{r}) - V_{xc}(\vec{r}))d^3r \tag{22}$$

is the contribution of exchange and correlation (see section 2.1.1). Hartree contribution to energy is the self-interaction energy of the density $n(\boldsymbol{r})$, when used as classical charge density:

$$E_{Hartree} = \frac{1}{2}\int d^3r d^3\acute{r}\frac{n(\boldsymbol{r})n(\boldsymbol{r'})}{|\boldsymbol{r}-\boldsymbol{r'}|} \tag{23}$$

Finally, E_{Ewald} is the electrostatic energy of atomic cores, that includes sum of interatomic interactions and self-energies:

$$E_{Ewald} = \frac{1}{2} \sum_{s,s'} Z_s Z_{s'} \sum_{T} \frac{1}{|R_{S'S}|} - \sum_{S} \frac{Z_S^2}{R_{C,S}} \tag{24}$$

Where Z_s is the charge of ions, S, $R_{S'S}$ is the distance between ions S' and S and $R_{C,S}$ the core radius of ions S.

First, we compare the coefficients of the total energy between the virtual atoms and the linear combination of the coefficients for Molybdenum and Tungsten atoms. The data are presented in Fig. 13.

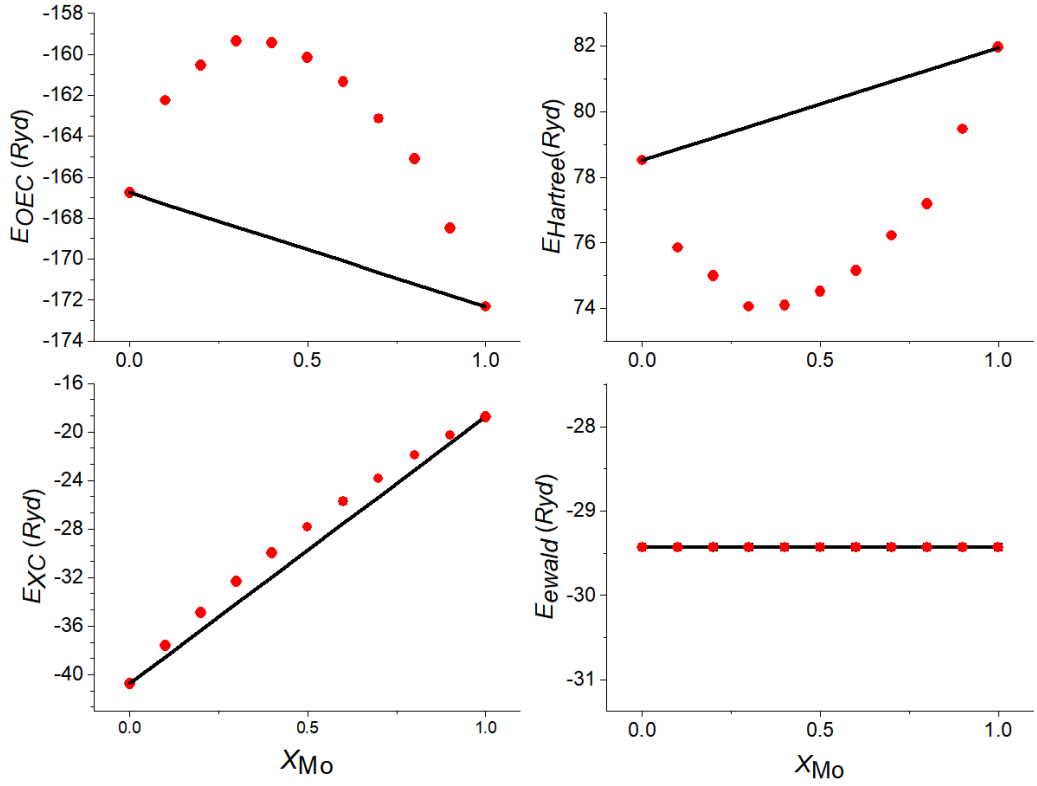

Figure 13: Contributions to total energy of an isolated Mo_xW_{1-x} atom as a function of x. The solid line is a linear interpolation between the end points.

There is a huge bowing effect for the one-electron contribution energy E_{OEC} and the Hartree energy coefficient $E_{Hartree}$. This is a clear indication of a bug in the software we use to create virtual atoms. The huge numbers in Fig. 13 show that there is not a satisfactory mixing of the two pseudopotentials . Although nuclear charge of virtual atoms is correct, as shown in the plot of Ewald, apparently electron density is not described correctly through VCA, resulting in strong non-linear behaviour of the Hartree energy. For this reason, we decided against using VCA for Mo_xW_{1-x} alloys.

On the contrary, mixture of S and Se creates virtual atoms which have intermediate properties between parent atoms, as shown in Fig. 14. Encouraged by these results, we will employ VCA to study nanostructures of S_xSe_{1-x} alloys.

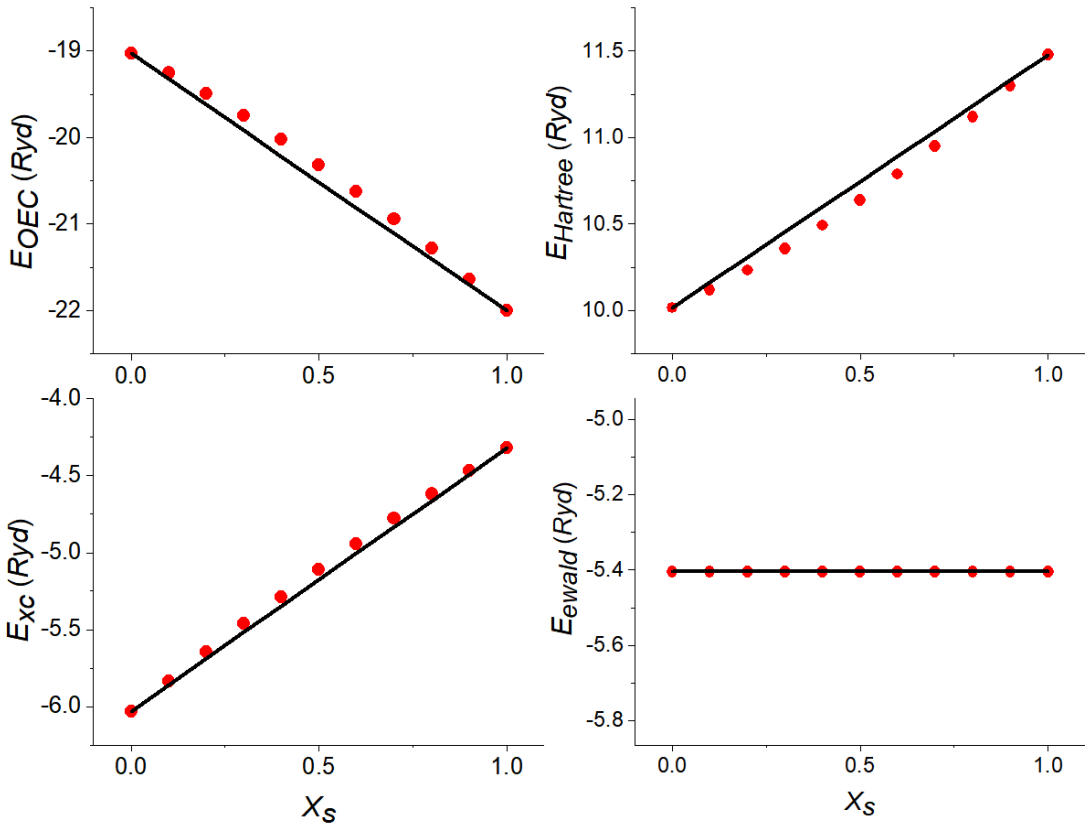

Figure 14: Contributions to total energy of an isolated S_xSe_{1-x} virtual atom as a function of x. The solid line is a linear interpolation between the end points.

4 Two-Dimensional Transition-Metal-Dichalcogenide Alloys

In this section we are going to use virtual crystal approximation in the calculation of band gap, lattice constant and the distance between the chalcogen atoms and compare it with other experimental and theoretical calculations as well as to our supercell calculations for some alloys to examine the general trend. For the supercell calculations, we used a supercell of 12 atoms which is the smallest possible supercell that gives overall good results.

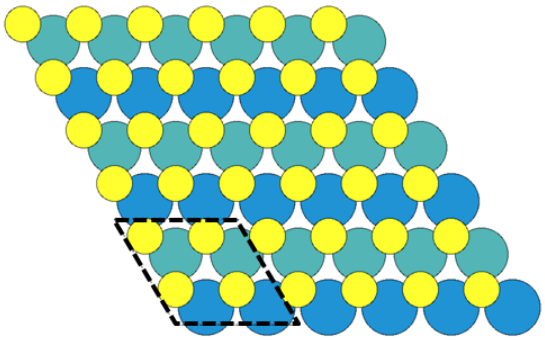

Figure 15: Top view of the supercell that consisted of 4 metal atoms (in blue and light blue) and 8 chalcogen atoms (in yellow) (dotted lines).Here, the $W_{0.5}Mo_{0.5}S_2$ structure is shown.

In order to calculate the band gap, we performed self consistent energy calcualtions for the minimum energy structure. The minimum energy structure is founded using the BFGS method. Also, we used the variable cell method to find the minimum energy cell for this structure. After that, we calculated the eigenvalues of energy for each k-point and we found the valence band maximum and the conduction band minimum. This methodology is employed for all band-gap calculations.

The structures we used in order to calculate the properties for the alloys using the supercell method are presented in Figure 16, together with the virtual crystal supercell (MoX_2).

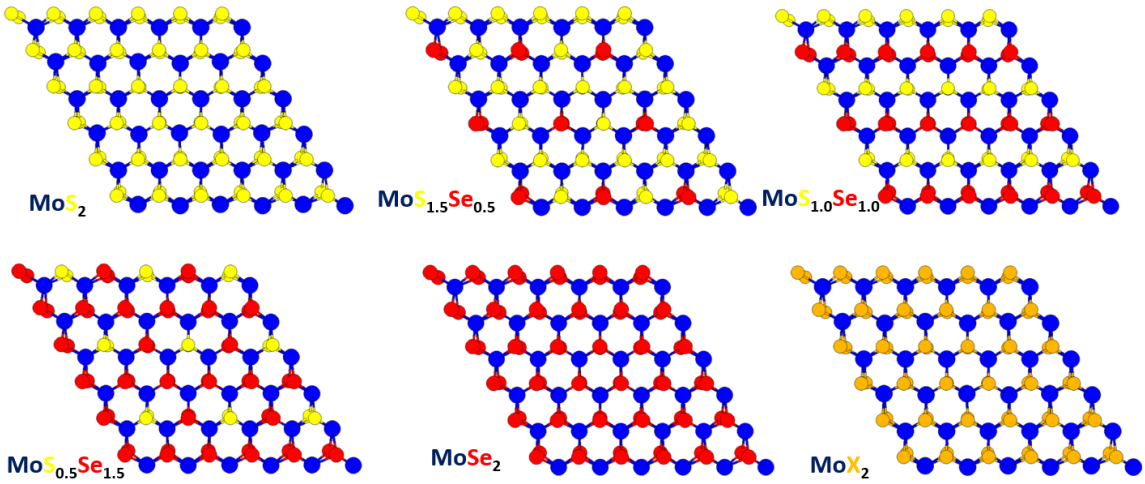

Figure 16: Top view of structures that made with the supercell method for MoS_xSe_{1-x} alloys. Color code: Mollybdenum (blue), Sulphur (yellow), Selenium (Red), Virtual atom S_xSe_{1-x} (Orange).

The band gap as a function of composition is presented in Fig. 17.

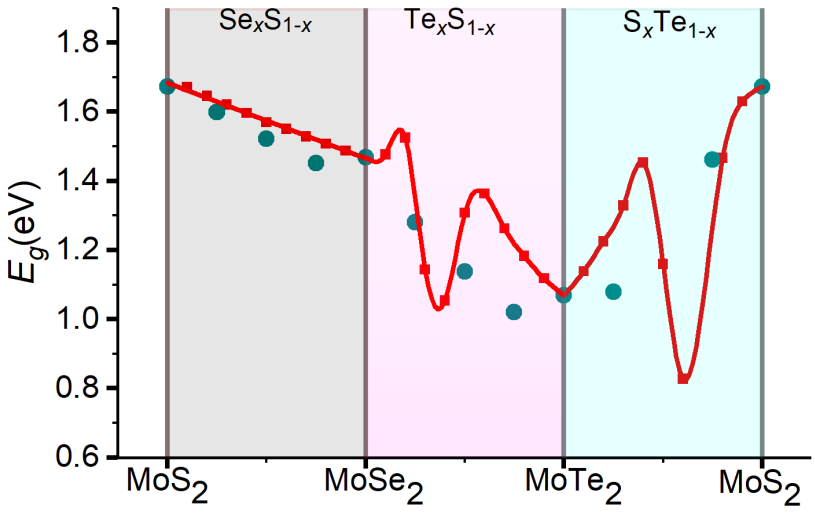

Figure 17: Band gap of TMD alloys as a function of concentration as calculated using the VCA approximation (red) and supercell method (blue). The continuous red line is a spline interpolation drawn to guide the eye. The pure materials are indicated by shaded lines

We see that the more matching trend between supercell and VCA simulations is between the MoS_2 and $MoSe_2$. In this region, gap is an almost linear function of composition as the Vegard's law suggests. Small deviation from linearity create a so-called bowing effect in agreement with experiments [12] and other simulations [13].

The distances between metal atoms and the distance between chalcogen atoms (d_{M-M} and d_{S-S}) in the minimum energy structure is presented in Figs 18 and 19. We find a perfectly linear dependence of distances on composition for S_xSe_{1-x} alloys. Again, Telluride alloys deviate significantly from linearity.

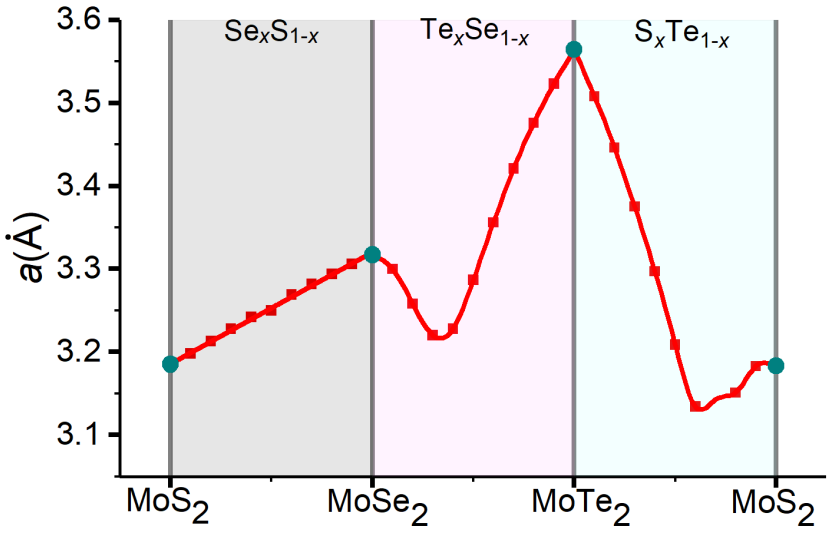

Figure 18: Lattice constant of TMD alloys as a function of concentration as calculated using the VCA approximation (red). The continuous red line is a spline interpolation drawn to guide the eye. The pure materials are indicated by shaded lines.

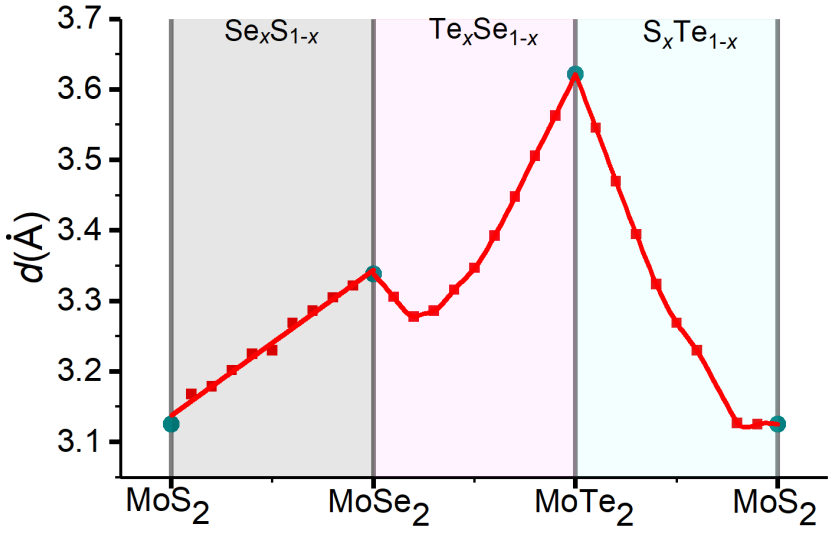

Figure 19: Distance between chalcogens of TMD alloys as a function of concentration as calculated using the VCA approximation (red). The continuous red line is a spline interpolation drawn to guide the eye. The pure materials are indicated by shaded lines.

We repeated the same calculations for tungsten dichalcogenides. The results are presented in Figs. 20,21 and 22.

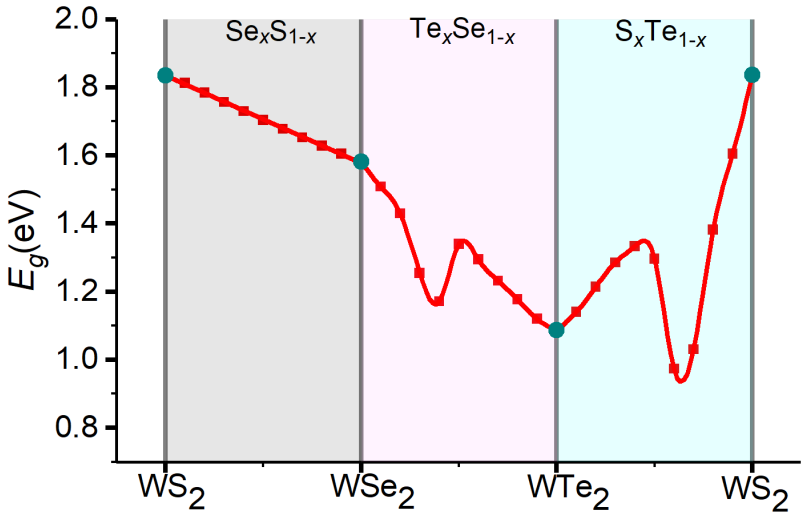

Figure 20: Band gap of TMD alloys as a function of concentration as calculated using the VCA approximation (red). The continuous red line is a spline interpolation drawn to guide the eye. The pure materials are indicated by shaded lines.

Similarly to the results for molybdenum dichalcogenides, we observe strong non-linearity in band gap and distances for Te-containing alloys. A similar, but not that dramatic, behaviour was observed in Ref. [2]. Unfortunately, there are no experimental data on Te-based alloys of TMDs, so it is not clear if this strong non linearity of properties is an artifact of the method we use or if it resembles an observed property of these materials.

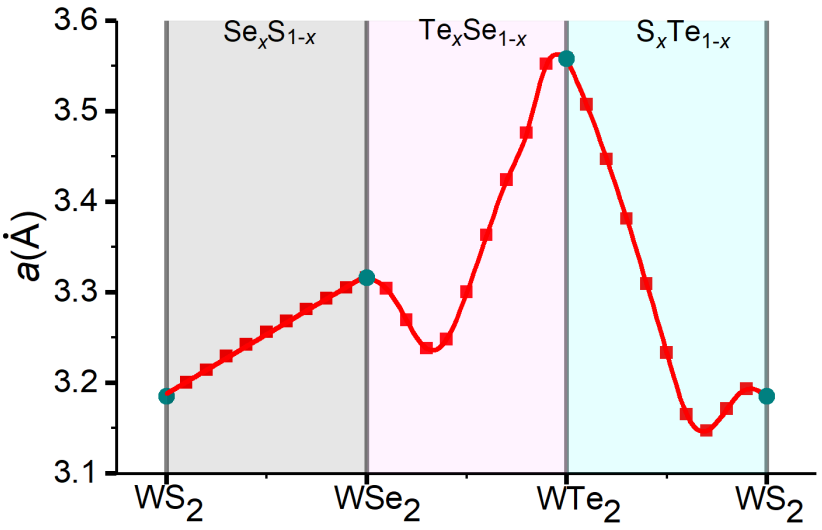

Figure 21: Lattice constant of TMD alloys as a function of concentration as calculated using the VCA approximation (red). The continuous red line is a spline interpolation drawn to guide the eye. The pure materials are indicated by shaded lines.

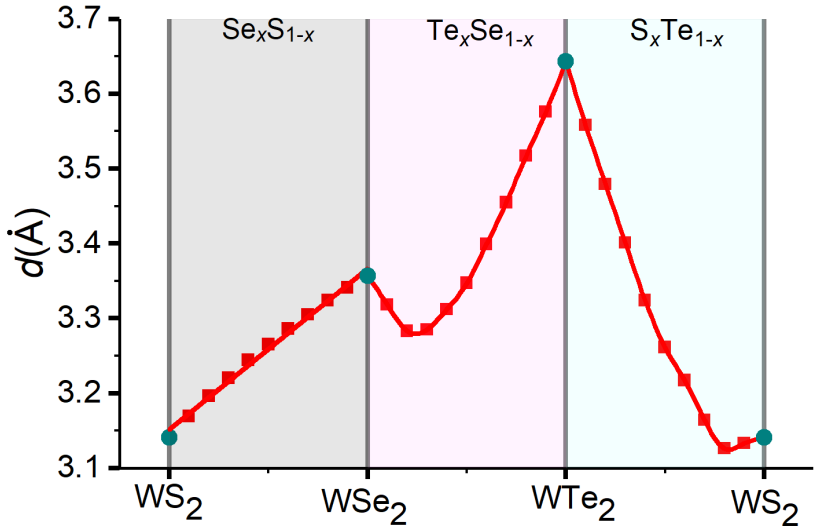

Figure 22: Distance between chalcogens of TMD alloys as a function of concentration as calculated using the VCA approximation (red). The continuous red line is a spline interpolation drawn to guide the eye. The pure materials are indicated by shaded lines.

Finally, we perform test calculations for the $W_xMo_{1-x}S_2$ band gap using VCA and supercell methods.

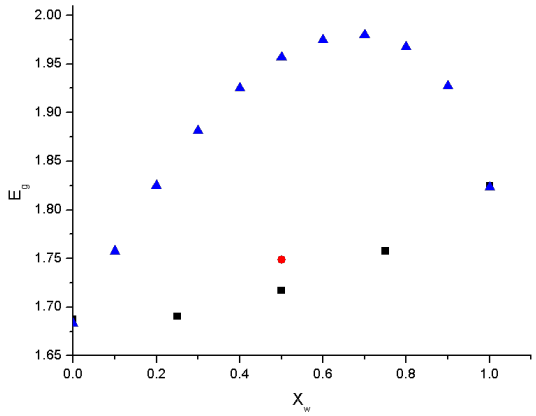

Figure 23: Band-gap for $W_xMo_{1-x}S_2$ as a function of x. Triangles: VCA calculations. Squares: Supercell calculations. Circle: Another structure to simulate MoSSe alloy with the supercell method.

The structures that we used in order to simulate the alloys with supercell method as well with VCA method are presented in Fig. 24, and the results for the band gap in Fig. 23.

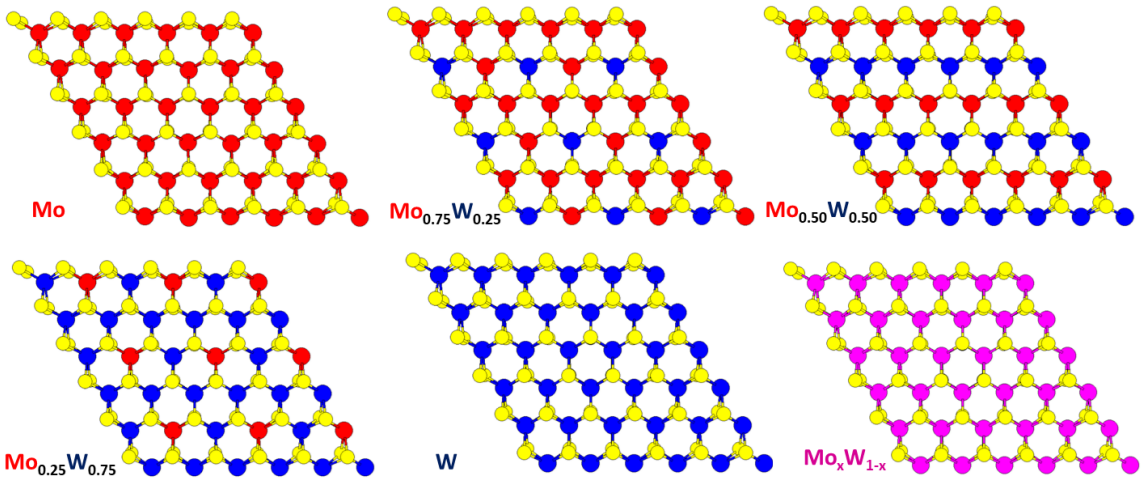

Figure 24: Top view of structures made with the supercell method for $W_{1-x}Mo_xS_2$ alloys. Color code: Mollybdenum (Red),Tungsten (Blue), Sulphur (yellow). Virtual atom (VCA) $W_{1-x}Mo_x$ (Pink).

The two different structures used to produce the two values of band gap are presented in the Fig. 25

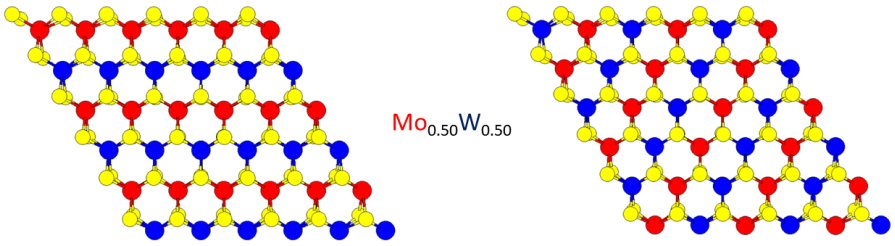

Figure 25: Two different supercells for the $W_{0.50}Mo_{0.50}S_2$ alloy.

The supercell structure gives the bowing type graph observed in experiments [13] and simulations. On the contrary, VCA gives a reverse bowing effect as shown in Fig. 23. This is a direct consequence of the problems encountered when mmixing the pseudopotentials for Mo and W (see section 3.2.1). We believe that the inability to mix the parent pseudopotentials in order to give better results for the one electron contribution energy and for the Hartreee contribution is the reason behind this disagreement with the other method. We can say that virtual crystal approximation method is not appropriate to use for calculations on transition metal alloys Mo_xW_{1-x}.

In conclusion, the VCA method produces excellent results for $MoS_{2x}Se_{2(1-x)}$ and $WS_{2x}Se_{2(1-x)}$. In these materials the band gap versus composition is almost linear and this behaviour agrees with the data that we have from previous researches [32] [9] and other calculations. Overall, we can say that we have a good basis for the next section's research.

5 Properties of $MoS_{2x}Se_{2(1-x)}$ Nanoribbons.

In this section, we present results of simulations for nanoribbons of $MoS_{2x}Se_{2(1-x)}$ alloys. In particular, we calculated the density of states and the formation energy for these alloys. Finally we discuss differences between segregated and random alloys.

Our simulation cell contains 38 atoms; twelve Mo units plus two X adatoms on the Mo edge. This termination is the most stable structure for the zig zag Mo edge [14]. We used the same unit cell as as in Ref [14]. We used variable cell relaxation and atomic relaxation through the BFGS algorithm in order to find the minimum energy structure. In order to simulate this materials we used 53.074 Ry or 725 eV cut off and $4 \times 1 \times 1$ k-point mesh.

We start by reproducing the end points of our space, MoS_2 and $MoSe_2$. In previous studies, nanoribbons of MoS_2 and $MoSe_2$ were found to have 3 states inside the band gap of the corresponding 2D material. Also, the Fermi energy of the nanoribbons was found to be lower than that of the 2D material [14].

For both nanoribbon and 2D structure, we calculate the electronic Density of States (DOS). We align the DOS of the nanoribbon with the DOS of 2D MoS_2 by taking into account the core s states that lie at energies about 15 eV below the Fermi level. In this way, we can calculate the Fermi level pinning, which is the difference between Fermi energy of the nanorribon and the Fermi energy of the 2D material.

5.1 MoS_2 nanoribbon.

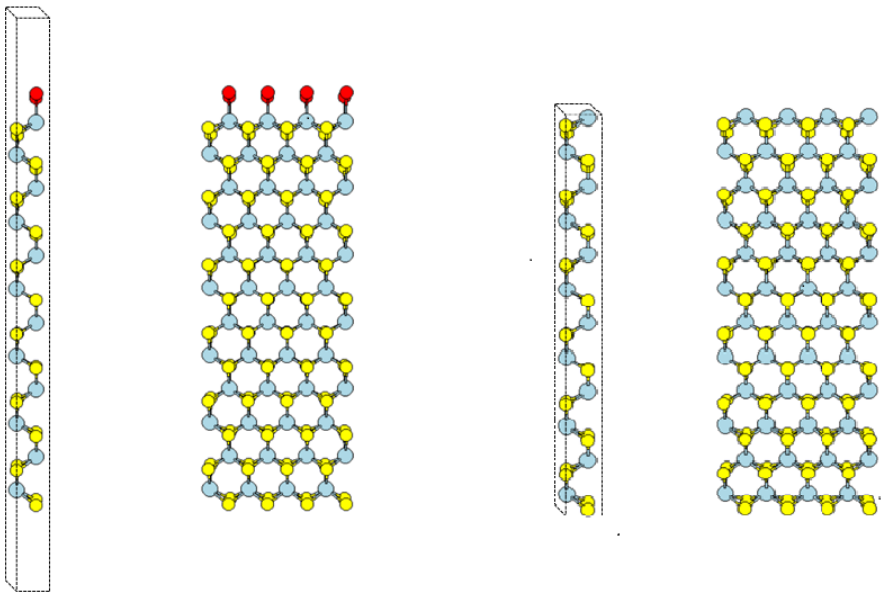

Figure 26: Left: Side view of the supercell for zig zag nanoribbon and 4×1 repetition that shows the generated structure. Right: Side view of the supercell with 36 atoms for 2D MoS_2 and 4×1 repetition that shows the generated structure. Color code: Transition metal (blue) , Chalcogens (yellow), Adatoms (Red)

Fig. 26 shows the unit cell of zig-zag MoS_2 nanoribbon with 3.183 Å width, and two adatoms that decorate the Mo edge. Fig. 26 shows a similar unit cell that can be used to study the infinite 2D material.

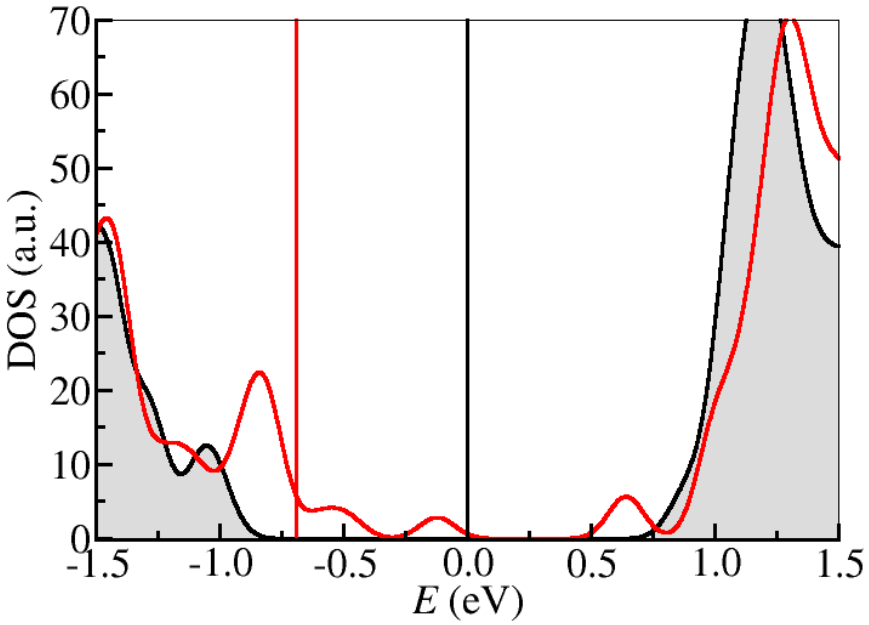

Figure 27: Electron Density of States (DOS) for MoS_2 nanoribbon (red) and infinite layer (black). The vertical lines denote the positions of the Fermi levels of the corresponding system.

Electronic Density of States graph (DOS) is shown in Fig. 27. In excellent agreement to previous works [14] we find 4 states inside the band gap of the 2D material in similar energies. Also, the Fermi energy that we calculated is the same that of [14]. This is a non-trivial result, given the difference of the simulation method of the present thesis and [14]: Quantum Espresso vs GPAW code, plane wave expansion vs real-space grid, and ultrasoft pseudopotentials vs projected augmented waves, just to name a few. So, we have strong evidence that our calculations are accurate.

Having established that our method produces excellent results (a) for $MoS_{2x}Se_{2(1-x)}$ alloys and (b) for MoS_2 and $MoSe_2$ nanoribbons, we are confident to proceed to the main task of this work, which is the study of nanoribbons of alloys.

5.2 $MoS_{2x}Se_{2(1-x)}$ nanoribbons with uniform composition.

In this subsection we simulate nanoribbons of alloys $MoS_{2x}Se_{2(1-x)}$ for several different concentrations (x). We use same unit cell and other computational parameters as those used for the study of MoS_2 nanoribbons presented in section 5.1. The only difference is that we substitute S atoms by virtual S_xSe_{1-x} atoms. Densities of states for the alloyed nanoribbons are shown in Fig. 28.

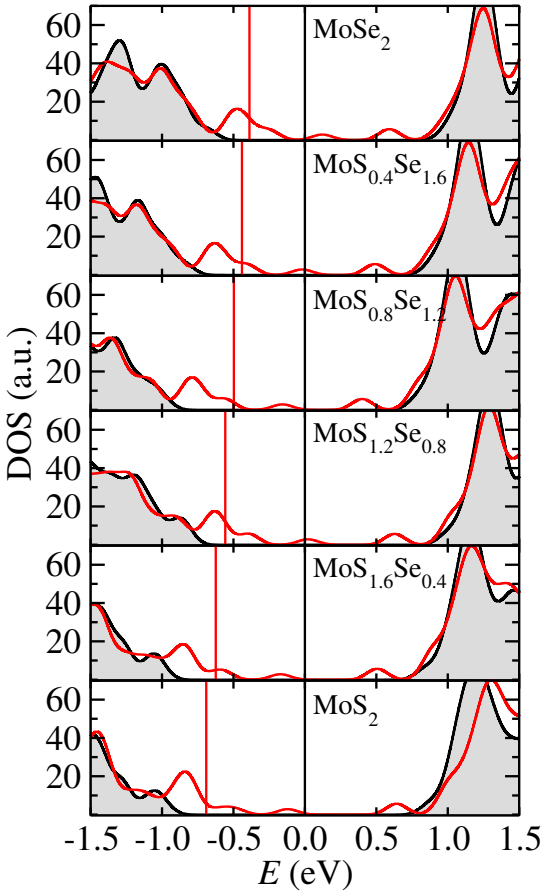

Figure 28: Electron Density of States (DOS) for alloys nanoribbon (red) and infinite layer (black). The vertical lines denote the positions of the Fermi levels of each material. For each alloy, zero in energy correspond to the Fermi level of the infinite 2D material.

In all cases, we find states inside the band gap of the 2D materials. The position of the nanoribbon states inside the band gap and the position of the Fermi level indicates that all nanoribbons have metallic character, in contrast to the 2D materials which are all semiconducting. Also, we find that the Fermi energy of the alloy is inside the band gap of the corresponding 2D material.

Interestingly, the band edges (valence band maximum and conduction band minimum) do not change monotonically as the alloy changes from MoS_2 to $MoSe_2$. On the other hand, as was the case with band gap (see Fig. 17), the Fermi level drops monotonically from -0.4 for $MoSe_2$ to -0.7 for MoS_2 with respect to the 2D material.

This pinning of Fermi level indicates that the states introduced in the gap will be occupied and the nanoribbon will be polarized with excess negative charge at its edges. The Fermi level pinning as a function of composition is shown in Fig. 30. An impressive linear dependance is found. This is an unexpected result, and might be useful property to keep in mind when designing nanostructures of TMD alloys.

To check the stability of alloy edges, we calculate the edge energy of the alloys. This can be derived from the total energies of the nanoribbon, E_{ribbon} and the 2D alloy, using the definition

$$\gamma = \frac{E_{ribbon} - E_{2D} - 2\mu}{2\alpha} \tag{25}$$

where E_{ribbon} is the total energy of the ribbon. E_{2D} is the total energy of 2D material with same number of atoms as the nanoribbon (see Fig. 26), and α is the lattice constant, μ is the chemical potential of the chalcogens; this term accounts for the energy of the two adatoms. The chemical potential can have any value between the energy per atom of gas-phase x and the energy per atom of solid x, where x is the virtual atom S_xSe_{1-x}. Here, we only consider atoms of x at zero temperature, so μ is the total energy of an isolated x atom, as given by DFT.

System	E_{tot} (Ry)	E_F^o (eV)	$\gamma(eV/\mathring{A})$	ϵ_c (eV/atom)
MoS_2 (nr)	-2208.62473751	-0.6907	-0.912	-6.82
MoS_2 (2D)	-2167.67427246	1.5467		-7.04
$MoS_{1.6}Se_{0.4}$ (nr)	-2206.62240246	-0.6238	-0.851	-6.66
$MoS_{1.6}Se_{0.4}$(2D)	-2165.81634632	1.6591		-6.88
$MoS_{1.2}Se_{0.8}$ (nr)	-2206.08251968	-0.5574	-0.815	-6.52
$MoS_{1.2}Se_{0.8}$(2D)	-2165.30224414	1.4826		-6.74
$MoS_{0.8}Se_{1.2}$(nr)	-2206.84422821	-0.4975	-0.788	-6.41
$MoS_{0.8}Se_{1.2}$(2D)	-2165.99054683	1.6809		-6.62
$MoS_{0.4}Se_{1.6}$(nr)	-2208.87200485	-0.4406	-0.766	-6.31
$MoS_{0.4}Se_{1.6}$(2D)	-2167.84876624	1.5666		-6.52
$MoSe_2$(nr)	-2212.16418954	-0.3879	-0.750	-6.23
$MoSe_2$(2D)	-2170.87554332	1.4480		-6.44

Table 3: Table of total energy, Fermi energy(as calculated before band aligment),cohesive energy and edge energy for $MoS_{2x}Se_{2(1-x)}$ nanoribbons (nr) and 2D structures.

Results for edge energies, γ, are presented in Table 3 and are plotted in Fig. 31. We find that edge energy is highest for $MoSe_2$ and drops at intermediate compositions before obtaining its minimum value for MoS_2. It is well known that MoS_2 is the most stable TMD material, and this is reflected to the fact that it has the most stable edges. On the other hand, all edge energies are negative, meaning that the 2D materials are unstable with respect to a gas of chalcogen atoms.

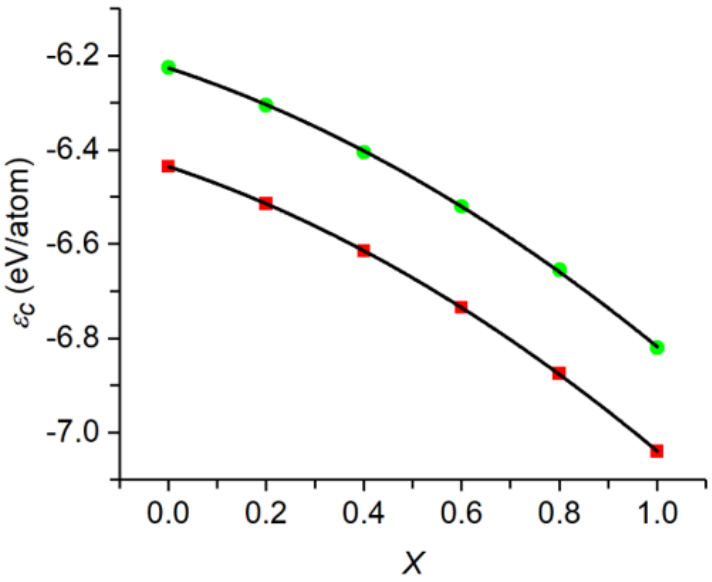

Figure 29: Cohesive energy for the nanoribbon and 2D of $MoS_{2x}Se_{2(1-x)}$ as a function of composition, x. Green circles are the nanoribbon. The red squares are the 2D. The black lines are a polynomial fit of the data. Nanoribbon : $\epsilon_c = -6.81 + 0.83X - 0.25X$. 2D : $\epsilon_c = -7.03 + 0.85X - 0.26X$.

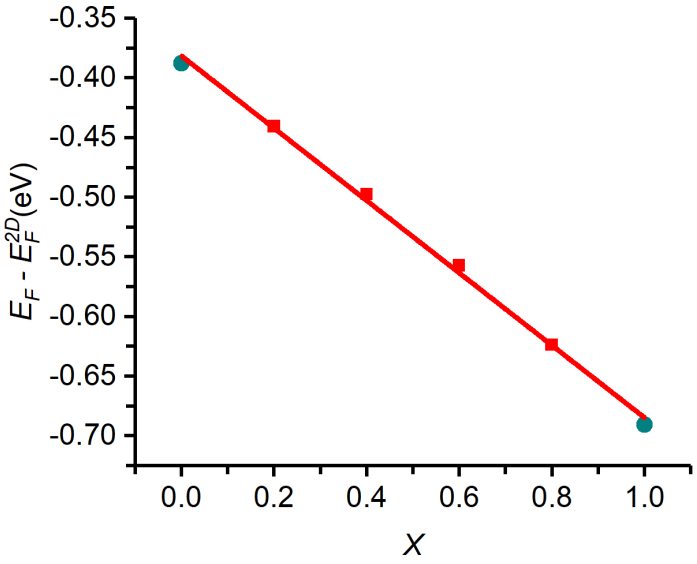

Figure 30: Fermi energy for the nanoribbon of $MoS_{2x}Se_{2(1-x)}$ as a function of composition, x. Blue circles are the pure materials. The red line is a linear fit of the data of the form of $E_F - E_F^{2D} = -0.38 - 0.30X$.

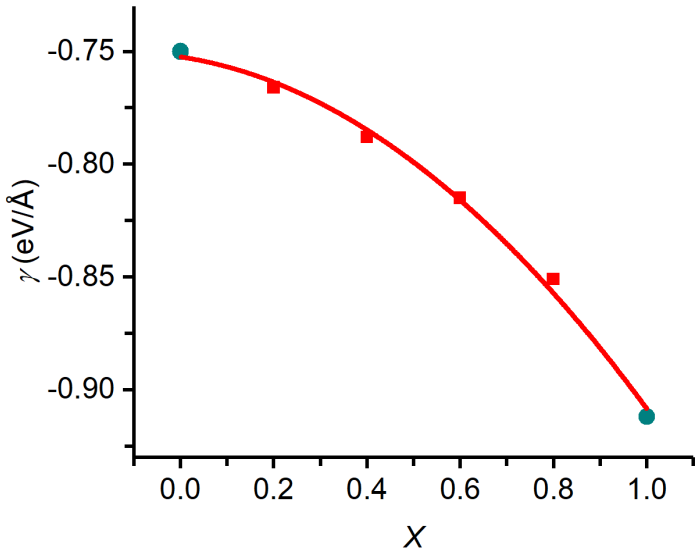

Figure 31: Edge energy of $MoS_{2x}Se_{2(1-x)}$ as a function of composition, x. Blue circles are the pure materials. The red line is a polynomial fit of the data of the form of $\gamma = -0.75 - 0.03x - 0.12x^2$.

5.3 $MoS_{2x}Se_{2(1-x)}$ nanoribbons with S-rich or Se-rich edges

In many cases, semiconductor alloys exhibit segregaton at their edges. A well-known example is Si_xGe_{1-x} nanostructure that always have Ge-rich surfaces and Si-rich covers. [33] Guided by this example, we now study nanoribbons that have overall composition close to $S_{0.5}Se_{0.5}$, and three regions: surfaces have one element only, core has the other element, and there is an intermediate region made of virtual atoms $S_{0.5}Se_{0.5}$. So what we made is a nanoribbon which on the outer region has sulphur or selenium while on the core it has selenium or sulphur, respectively. For example if the outer region is sulphur then the core is selenium. The middle area is a combination of sulphur and selenium by $50-50\%$. The structure is shown in Fig. 32. The unit cell contains 12 Mo atoms and 26 chalcogen atoms: 12 virtual atoms $S_{0.5}Se_{0.5}$, 8 atoms of one kind and 12 atoms of the other.

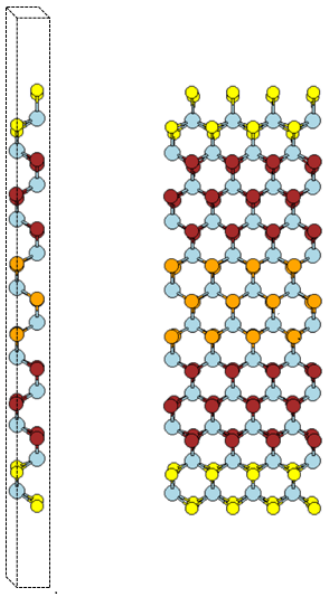

Figure 32: Segregated nanoribbon with three types of atoms: The orange atoms(core) will be sulphur or selenium, the red atoms (middle) will be virtual atoms $S_{0.50}Se_{0.50}$ and the yellow atoms(outer) will be either sulphur or selenium.

Depending on whether the majority chalcogen is S or Se, we made two types of alloys with similar composition: on one the majority element is the

selenium($MoS_{0.92}Se_{1.08}$) and on the other the majority element is the sulphur ($MoS_{1.08}Se_{0.92}$). For each concentration we made two different structures with different arrangement of the atoms, one with sulphur on the edges and one with selenium on the edges. In all cases, we fully relax the atomic positions and the lattice constants to ensure that the system is at it's lowest energy structure. For comparison, we created two nanoribbons with uniform composition where all atoms are identical virtual atoms $S_{0.46}Se_{0.54}$ or $S_{0.54}Se_{0.46}$.

For each system, we calculate the cohesive energy per atom, ϵ_c, defined as

$$\epsilon_c = \frac{E_{total} - N_{Mo}E_{Mo} - N_S E_S - N_{Se}E_{Se} - N_V E_V}{38} \tag{26}$$

where E_{total} is the total energy of the nanoribbon cell, N_{Mo}, N_S, N_{Se}, N_V is the number of Mo, S, Se and virtual atoms and E_{Mo}, E_S, E_{Se}, E_V is the energy of Mo,S,Se and virtual atoms, respectively. The denominaton ,38, is the total number of atoms in the nanoribbon.

System	E_{tot} (Ryd)	ϵ_c (eV/atom)
$MoS_{1.08}Se_{0.92}$ (nr, S edges)	-2208.30985740	-6.49
$MoS_{1.08}Se_{0.92}$ (nr, Se edges)	-2209.01477527	-6.53
$MoS_{1.08}Se_{0.92}$ (nr, uniform)	-2206.16134140	-6.48
$MoS_{1.08}Se_{0.92}$ (2D)	-2165.38421274	-6.70
$MoS_{0.92}Se_{1.08}$ (nr, S edges)	-2209.20713061	-6.46
$MoS_{0.92}Se_{1.08}$ (nr, Se edges)	-2208.65794222	-6.48
$MoS_{0.92}Se_{1.08}$ (nr, uniform)	-2206.47054852	-6.43
$MoS_{0.92}Se_{1.08}$ (2D)	-2165.75817214	-6.69

Table 4: Total and cohesive energies of nanoribbon (nr) and 2D materials close to $S_{0.5}Se_{0.5}$ composition.

Looking at the cohesive energies presented in table 4, we note that the 2D materials have always lower energy than nanoribbons, as a consequence of the energy of the broken bonds at the edges. As Se has lower cohesive energy than S, structures with more Se have higher energy. In both compositions the nanoribbons that have sulphur as core are more stable than those of selenium core. This is another consequence of the lower cohesive energy of Se.

In all cases, the segregated alloy is more stable than the random alloy. However, the gain in energy due to segregation is very small (of the order of few meV per atom).

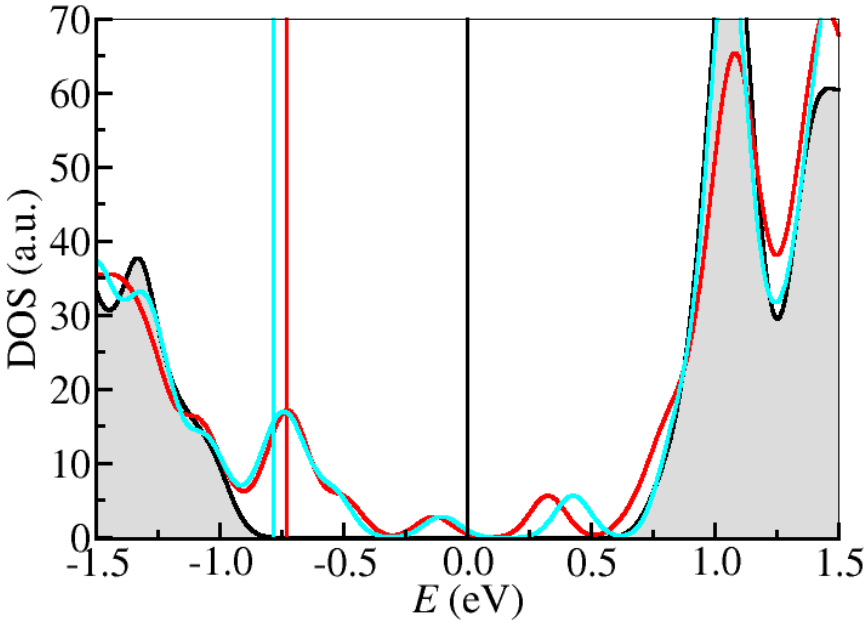

Figure 33: Electron Density of States (DOS) for $MoS_{1.08}Se_{0.92}$ uniform composition nanoribbon (red), mixed method nanoribbon with Se edges and S core (cyan). A 2D layer with same composition is also shown (black). The vertical lines denote the positions of the Fermi levels of the corresponding DOS.

In addition to lower cohesive energy, segregated alloy has lower Fermi level than the uniform alloy, as shown in Fig. 33. Again, the difference in DOS between uniform composition and Se-rich edges is small, so we suggest that VCA can be used for a quick calculation of electronic structure of nanostructures.

In other words, the segregated and the random alloys do not have much difference as for the density of states diagram. So we can say safely that a virtual crystal is a good simplification of the more realistic problem of the segregated alloy.

In Fig. 34, we visualize the electron wave function of a state close to the Fermi level. We observe that electrons accumulate on the edge of the nanoribbon. Such states were observed in MoS_2 nanoribbons and have been studied extensively theoretically [6]. They have true metallic character. Electrons are strongly localized within about 5 Åof the edge [6], but on the other hand they are totally delocalized along the edges.

We verify that these very interesting edge states are also present in TMD alloys.

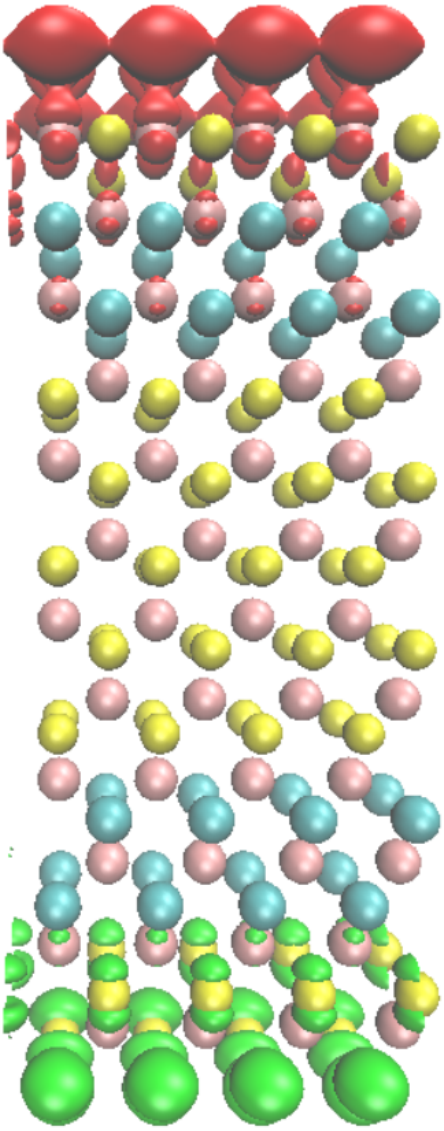

Figure 34: Wave functions of Kohn-Sham states for segregated $MoS_{1.08}Se_{0.92}$ 2D alloy Nanoribbon localized on the edges of the nanoribbon. Spheres represent atoms. Two states are plotted, one at exactly the Fermi level (red) and one which lied few meV lower in energy.

6 Conclusions and outlook

The aim of this study was to study the electronic structure of edges of TMD alloys, with a method that balances between accuracy and efficiency. We used Density functional Theory for electronic structure calculations and Virtual Crystal Approximation for the creation of the alloys. We achieved reliable results with respect to other experimental and accurate computationall methods.

We calculate the electronic and structural parameters for pure materials in excellent agreement with the literature. We found linearity for the band gap as a function of the composition for alloys of MoS_2 and $MoSe_2$ in agreement with other researchers and with supercell calculations. Unfortunately, the method is problematic when applied to Mo_xW_{1-x} or Te-containing alloys.

For MoS_2 and $MoSe_2$ nanoribbons we also find results in excellent agreement with other researchers. The simulations for $MoS_{2x}Se_{2(1-x)}$ nanoribbons produced very interesting results. In all cases we find states inside the band gap of the 2D material. The position of Fermi level together with Density of States and wavefunction plots confirm the metallic character of the nanoribbon alloys in contrast to 2D material. An impressive linear dependance is found between the Fermi level pinning and the composition, which is a an unexpected result. Also, the states introduces in the gap will be occupied and the nanoribbon will be polarized with excess negative charge at its edges.

Considering nanoribbons of S-Se alloys with non-uniform composition, simulating a nanoribbon with three different areas of atoms. For each system we found that the more stable nanoribbons are the ones with S-rich core and Se-rich edges, in accordance with other semiconductor alloy nanostructures where usually the heavier elements dominate the surfaces.

The most striking finding of this study was the fact that simple VCA gives accurate results for very complex systems, such as nanoribbons of alloys. Even for a segregated alloy with five different composition domains, VCA gives correct results for the cohesive energy and the position of the Fermi level up to few tens of meVs. This finding shows that the method used in this thesis is an extremely powerful tool for the computer-aided design of TMD nanoalloys.

7 References

References

[1] W. Kohn. Nobel Lecture : Electronic Structure of Matter — Wave Functions and Density Functionals, 1999.

[2] H. P. Komsa and A. V. Krasheninnikov. Two-dimensional transition metal dichalcogenide alloys: Stability and electronic properties. *Journal of Physical Chemistry Letters*, 3:3652–3656, 2012.

[3] A. K. Geim and K. S. Novoselov. The rise of graphene. *Nature Materials*, 6:183–191, 2007.

[4] P. K. Ahluwalia A. Kumar. Electronic structure of transition metal dichalcogenides monolayers 1H-MX2 (M = Mo, W; X = S, Se, Te) from ab-initio theory: new direct band gap semiconductors. *The European Physics Journal B*, 85:186, 2012.

[5] A. K. J. N. C. M. S. Strano H. Wang, K. Kalantar-Zadeh. Electronics and optoelectronics of two-dimensional transition metal dichalcogenides. *Nature Nanotechnology*, 7:699–717, 2012.

[6] D. Davelou, G. Kopidakis, G. Kioseoglou, and I. N. Remediakis. MoS_2 nanostructures: Semiconductors with metallic edges. *Solid State Communications*, 192:42–46, 2014.

[7] J. Jia, F. Xu, S. Wang, X. Jiang, Z. Long, and X. Hou. Two-dimensional MoS_2 nanosheets as a capillary GC stationary phase for highly effective molecular screening. *The Analyst*, 139:3533–3536, 2014.

[8] K. F. Mak, C. Lee, J. Hone, J. Shan, and T. F. Heinz. Atomically thin MoS_2: A new direct-gap semiconductor. *Physical Review Letters*, 105:136805, 2010.

[9] A. E. Maniadaki, G. Kopidakis, and I. N. Remediakis. Strain engineering of electronic properties of transition metal dichalcogenide monolayers. *Solid State Communications*, 227:33–39, 2016.

[10] B. S. Massoth F. E. Topsøe, H. Clausen. Hydrotreating Catalysis, Science and Technology. *Springer-Verlag*, 1996.

[11] F. L. Claus. Solid Lubricants and Self-Lubricating Solids. *New York: Academic Press*, 1972.

[12] H. Li, X. Duan, X. Wu, X. Zhuang, H. Zhou, Q. Zhang, X. Zhu, A. Pan, and Xiangfeng D. Growth of Alloy $MoS_{2x}Se_{2(1-x)}$ Nanosheets with Fully Tunable Chemical Compositions and Optical Properties. *Journal of the American Chemical Society*, 136:3756–3759, 2014.

[13] S. Susarla, A. Kutana, J. A. Hachtel, V. Kochat, A. Apte, R. Vajtai, J. C. Idrobo, B. I. Yakobson, C. S. Tiwary, and P. M. Ajayan. Quaternary 2D Transition Metal Dichalcogenides (TMDs) with Tunable Bandgap. *Advanced Materials*, 35, 2017.

[14] D. Davelou, G. Kopidakis, E. Kaxiras, and I. N. Remediakis. Nanoribbon edges of transition-metal dichalcogenides: Stability and electronic properties. *Physical Review B*, 96:165436, 2017.

[15] M. V. Bollinger, J. V. Lauritsen, K. W. Jacobsen, J. K. Nørskov, S. Helveg, and F. Besenbacher. One-dimensional metallic edge states in MoS_2. *Physical Review Letters*, 87:196803, 2001.

[16] J. C. Slater. A simplification of the Hartree − Fock method. *Physical Review Letters*, 81:385–390, 1951.

[17] W. Kohn and L. J. Sham. Self-Consistent Equations Including Exchange and Correlation Effects. *Physical Review Letters*, 140:A1133–A1138, 1965.

[18] P. Hohenberg and W. Kohn. Inhomogeneous electron gas. *Physical Review Letters*, 136:B864–B871, 1964.

[19] J. P. Perdew, K. Burke, and M. J. Ernzerhof. Generalized Gradient Approximation Made Simple. *Physical Review Letters*, 77:3865–3868, 1996.

[20] D. R. Hamann, M. Schlüter, and C. Chiang. Norm-conserving pseudopotentials. *Physical Review Letters*, 43:1494, 1979.

[21] K. F. Garrity, J. W. Bennett, K. M. Rabe, and D. Vanderbilt. Pseudopotentials for high-throughput DFT calculations. *Computational Materials Science*, 81:446–452, 2014.

[22] D. Vanderbilt. Soft self-consistent pseudopotentials in a generalized eigenvalue formalism. *Physical Review B*, 41:7892, 1990.

[23] C. Payne. Iterative minimization techniques for ab initio total-energy molecular dynamics and conjugate gradients calculations. 64:1045, 1992.

[24] E. Kaxiras. *Atomic and Electronic Structure of Solids*. Cambridge University Press, 2003.

[25] L. Bellaiche and D. Vanderbilt. Virtual crystal approximation revisited: Application to dielectric and piezoelectric properties of perovskites. *Physical Review B*, 61:7877–7882, 2000.

[26] S. de Gironcoli, P. Giannozzi, and S. Baroni. Structure and thermodynamics of Si_xGe_{1-x} alloys from ab initio Monte Carlo simulations. *Physical Review Letters*, 66:2116, 1991.

[27] F. M. Armando and S. Fahy. First-principles calculation of alloy scattering in Ge_xSi_{1-x}. *Physical Review Letters*, 97:96606, 2006.

[28] R. Fletcher. *Practical Methods of Optimization (2nd Ed.)*. Wiley-Interscience, 1987.

[29] I. E. Castelli N. Mounet G. Prandini, A. Marrazzo and N. Marzari. http://materialscloud.org/sssp. *Computational Materials*, 2018.

[30] D. Y. Qiu, F. H. Da Jornada, and S. G. Louie. Optical spectrum of MoS_2: Many-body effects and diversity of exciton states. *Physical Review Letters*, 111:216805, 2013.

[31] R. M. Martin. *Electronic Structure: Basic Theory and Practical Methods*. Cambridge University Press, 2004.

[32] A. Kutana, E. S. Penev, and B. I. Yakobson. Engineering electronic properties of layered transition-metal dichalcogenide compounds through alloying. *Nanoscale*, 6:5820–5825, 2014.

[33] G. Vantarakis, I. N. Remediakis, and P. C. Kelires. Ordering mechanisms in epitaxial sige nanoislands. *Physical Review Letters*, 108:176102, 2012.